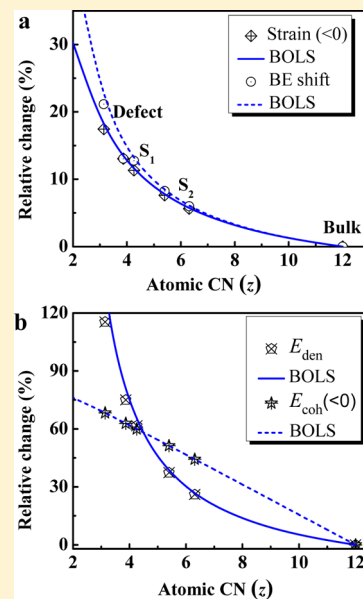


Bond Order Resolved $3d_{5/2}$ and Valence Band Chemical Shifts of Ag Surfaces and NanoclustersWei Qin,[†] Yan Wang,^{*,†,‡} Yongli Huang,[†] Zhaofeng Zhou,[†] Chao Yang,[†] and Chang Q. Sun^{*,†,§}[†]Institute for Quantum Engineering and Micro-Nano Energy Technology, Key Laboratory of Low-Dimensional Materials and Application Technologies, and Faculty of Materials, Optoelectronics, and Physics, Xiangtan University, Hunan 411105, China[‡]School of Information and Electronic Engineering, Hunan University of Science and Technology, Hunan 411105, China[§]School of Electrical and Electronic Engineering, Nanyang Technological University, Singapore 639798, Singapore

ABSTRACT: Incorporating the tight-binding theory and the bond order–length–strength (BOLS) correlation into the X-ray photoelectron spectra of Ag(111) and (100) surfaces and the Auger electron spectra of Ag nanoparticles deposited on Al_2O_3 and CeO_2 substrates has led to quantitative information of the $3d_{5/2}$ and the valence binding energies of an isolated Ag atom and their shifts upon bulk, defect, surface, and nanocrystal formation. It is clarified that the globally positive energy shifts originate from the undercoordination-induced Goldschmidt–Pauling bond contraction and the associated local quantum entrapment and the heterocoordination-induced bond nature alteration at the particle–substrate interfaces. Perturbation to the Hamiltonian by atomic ill-coordination dictates the energy shift that is proportional to the bond energy at equilibrium. Theoretical reproduction of the measured spectroscopic data derived that the $3d_{5/2}$ energy of an isolated Ag atom shifts from 363.02 to 367.65 eV and the valence band center from 0.36 to 8.32 eV upon bulk formation. The extended Wagner plots revealed the coefficients of valence recharging and potential screening to be 1.21 and 1.56 for Ag interacting with Al_2O_3 substrate and 1.15 and 1.50 for Ag with CeO_2 , respectively. Exercises exemplify the enhanced capabilities of XPS and AES in determining quantitative information regarding the evolution of the local bond length, bond energy, binding energy density, and atomic cohesive energy, with the coordination and chemical environment.



1. INTRODUCTION

Ag surfaces and nanoparticles (NPs) have inspired intensive research interest¹ because of their significance in both basic science and practical applications such as biochemistry and plasmonics due to their intriguing properties compared with those of the silver bulk. As the size decreases to nanoscale, a large fraction of undercoordinated atoms is generated. The interaction between the undercoordinated atoms dominates the properties of Ag NPs, defects, and surfaces and makes them different from their bulk counterpart. For example, the Raman signal of Ag NPs at a certain size range could be enhanced by 10 times to that of the corresponding bulk.² Pal et al.³ pointed out that the biocidal property of Ag is influenced by the size and shape of NPs. Because of the importance of electronic structure in electronic and optic properties of Ag, the evolution of the electronic binding-energy levels and the energy band configurations of the Ag NPs should be the key. Tremendous work has been done in this regard from both the theoretical and experimental perspectives.^{4–7} For instance, the size resolved core level shift and the MSVV Auger parameter shift of Ag NPs deposited on Al_2O_3 were observed using X-ray photoelectron spectroscopy (XPS) and Auger electron spectroscopy (AES). The observed energy shifts are generally ascribed as the final–

initial state relaxation in the process of ionization and excitation.^{8–10} Hernández et al.¹¹ found that the main contribution to core level shift is the charge transfer to the surface for Ag deposited on $\alpha\text{-Al}_2\text{O}_3$ by using spin-polarized density functional theory calculations, while Rodriguez et al.¹² concluded that the Ag $3d_{5/2}$ binding energy (BE) shift cannot be attributed to the formation of Ag–O bond at surface from their thermal desorption mass spectroscopy investigation. Although the unusual behavior of Ag at the undercoordinated sites has been intensively investigated, the mechanism behind these entities remains as yet unclear. Moreover, the effects of interface on core level shift and the correlation between the shifts of different bands have been rarely explored. Therefore, a consistent understanding of the effects of undercoordination and heterocoordination on the electronic BE shift is highly desired.

In this contribution, we report our findings in analyzing the XPS and AES of Ag surfaces and clusters under the framework of bond order–length–strength (BOLS) correlation¹³ and

Received: May 5, 2012

Revised: June 3, 2012



tight-binding (TB) theory. Theoretical reproduction of the XPS and AES measurements on the MSVV Auger kinetics energy, the $3d_{5/2}$ core level, and the valence band (VB) shift of Ag upon bulk, defect, surface, and nanocrystal formation leads to comprehensive knowledge about the respective energy shifts, local bond strain, binding energy density, and atomic cohesive energy in the skin up to two atomic layers. Meanwhile, we clarified that the globally positive energy shifts originate from the undercoordination-induced bond contraction, the associated local quantum entrapment, and the heterocoordination-induced bond nature alteration at the interfaces.

2. PRINCIPLES

2.1. Core-Level Shift (CLS). As illustrated in Figure 1, the following items have been clarified:^{14,15}

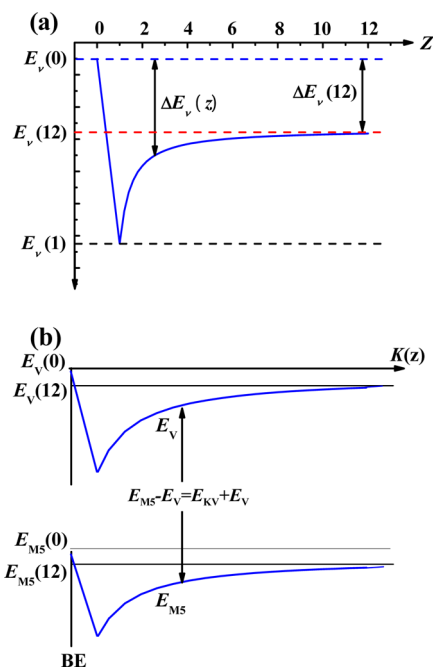


Figure 1. Illustration of (a) the core level of an isolated atom ($E_\nu(z=0)$) and its evolution ($E_\nu(z)$) with atomic CN. The energy shift $\Delta E_\nu(z) = E_\nu(z) - E_\nu(0)$ is proportional to the cohesive energy per bond at the equilibrium. (b) The rule of energy conservation of Ag MSVV Auger process. The energy separation $E_{MS} - E_\nu$ excites an electron at the KV level to escape the binding energy of E_{KV} and carries the rest of the Auger kinetic energy $E_\nu(K)$.

- The energy level of an isolated atom in the ν th core level, $E_\nu(0)$, determined by the intra-atomic interaction, should be the intrinsic reference point from which the CLS proceeds.
- The CLS arises intrinsically from the perturbation to the interatomic bonding energy in the Hamiltonian; the extent of the CLS is proportional to the cohesive energy per bond at equilibrium.
- The CLS is globally positive upon the bulk, defect, surface, and nanocrystal formation because of the involvement of interatomic interaction and the BOLS correlation.
- The extent of the CLS varies with atomic coordinate number (CN) that determines the bond length and bond energy; the CLS should be even more pronounced upon

atomic CN being reduced because of the bond order loss induced bond strength gain.

- The extrinsic effects of charge accumulation or the initial–final states relaxation during measurement can be minimized in calibration because these processes exist throughout the course of experiments.

According to the energy band theory of the TB approach,¹⁶ the energy shift of a specific ν th core band from that of an isolated atom is proportional to the local bond energy at equilibrium:

$$\begin{aligned} \Delta E_\nu(z) &= E_\nu(z) - E_\nu(0) \\ &= \langle \nu, i | V_{\text{cr}}(r) (1 + \Delta_H) | \nu, j \rangle \\ &\propto E_b (1 + \Delta_H) [1 + o(\langle \nu, i | \nu, j \rangle)] \\ \Delta_H &= \begin{cases} C_z^{-m} - 1 & (\text{ith atomic site}) \\ \tau K^{-1} \sum_{i \leq 3} C_z (C_z^{-m} - 1) & (\text{shell-resolved cluster}) \end{cases} \quad (1) \end{aligned}$$

The wave functions, for the core electrons at atomic sites i and j ($\langle \nu, i | \nu, j \rangle = \delta_{ij}$), are assumed to change little as they are strongly localized with insignificant overlapping. δ_{ij} is the Kronecker delta function: $\delta_{ij} = 1$ if $i = j$; otherwise, $\delta_{ij} = 0$. $E_\nu(0)$ is the ν th energy level of an isolated atom determined by the intra-atomic trapping potential. $\Delta E_\nu(z)$ is the shift of the ν th energy level of an atom with z coordination number ($E_\nu(z)$) from that of an isolated atom, $E_\nu(0)$. Any perturbation to the crystal potential, Δ_H , will shift the ν th core level $E_\nu(z)$ (band center) away from the $E_\nu(0)$ accordingly. $C_z = d_z/d_b = 2/\{1 + \exp[(12 - z)/(8z)]\}$ being the bond contraction coefficient is the z -dependent relative bond length^{17,18} and $C_z^{-m} = E_z/E_b$ is the relative bond energy or the relative depth of the quantum trap potential.¹⁵ τ is the shape factor ($\tau = 1, 2$, and 3 corresponds to a thin plate, a cylindrical rod, and a sphere dot, respectively). K being the dimensionless form of size is the number of atoms lined along the radius of a nanoparticle.

Generally, an XPS spectrum providing broad peaks of the core-levels can be decomposed into several Gaussian peaks, which represent contributions from different z -coordinated atoms. These components are therefore correlated by¹⁴

$$\frac{E_\nu(z) - E_\nu(0)}{E_\nu(12) - E_\nu(0)} = \frac{E_z}{E_b} = C_z^{-m} = 1 + \Delta_H \quad (2)$$

With the given energies of XPS components of z and z' in decomposition, we can determine the referential $E_\nu(0)$ and the bulk shift, $\Delta E_\nu(B)|_{z=12} = \Delta E_\nu(12) = E_\nu(12) - E_\nu(0)$:

$$\begin{aligned} \frac{E_\nu(z) - E_\nu(0)}{E_\nu(z') - E_\nu(0)} &= \frac{C_z^{-m}}{C_{z'}^{-m}} \text{ or } E_\nu(0) \\ &= \frac{C_{z'}^m E_\nu(z') - C_z^m E_\nu(z)}{C_{z'}^m - C_z^m} \quad (3) \end{aligned}$$

$$E_\nu(z) - E_\nu(0) = [E_\nu(12) - E_\nu(0)] C_z^{-m} \quad (4)$$

In fact, bonds at the surface are shorter^{3,19,20} and stronger, which dominate the size effect on the CLS, while bonds in the core interior remain their bulk nature. Using the sum rule of the core–shell structure and taking the surface-to-volume ratio into effect, we can deduce the K dependence of ν th energy level $E_\nu(0)$ and its bulk shift $\Delta E_\nu(12)$

$$E_v(K) = E_v(0) + [E_v(12) - E_v(0)] \times [\tau K^{-1} \sum_{i \leq 3} C_z(C_z^{-m} - 1)] \quad (5)$$

Generally, the size-induced shifts of the BE nanoparticles exhibit an inverse linear size relationship. For example, Yang et al.²¹ reported the shift of binding energy in Cu LMM Auger process following the $1/K$ scaling relationship with a slope sensitive to processing conditions and substrate material when Cu is deposited on highly oriented pyrolytic graphite. The form is $E_v(K) = A + BK^{-1}$, where A and B are constants that can be determined by finding the intercept and the gradient, respectively. Comparing the experimental scaling relationship with the theoretical expression derived from eq 5 yields

$$\begin{cases} A = E_v(0) \\ B = [E_v(12) - E_v(0)]\tau \sum_{i \leq 3} C_z(C_z^{-m} - 1) \end{cases} \quad (6)$$

Then, we can obtain the shape factor τ of the sample:

$$\tau = B / \left\{ [E_v(12) - E_v(0)] \sum_{i \leq 3} C_z(C_z^{-m} - 1) \right\} \quad (7)$$

With the derived $E_v(12)$, $E_v(0)$, m , and the given z values for the outermost three atomic layers, we are able to decompose the measured XPS spectra into the corresponding surface and bulk counterparts.

2.2. Energy Conservation in the Auger Process. In an Auger process of Ag, for example, the M5VV denotes the process of electron transition between the deeper $3d_{5/2}$ (M5) and upper valence level (V) and emits the Auger electrons with kinetic energy (KV). The energy conservation in the Auger process and the Auger parameter follow the relationships (Figure 1b)²²

$$\begin{cases} E_{M5} - E_V = E_{KV} + E_V \\ \text{(energy conservation)} \\ \alpha' = E_{KV} + E_{M5} \quad \text{(Auger parameter)} \end{cases}$$

Considering the absolute magnitudes of the energies and the referencing point to the specific energy level of an isolated atom, the magnitude of Auger parameter shift is actually twice the shift of the double-hole V level, ΔE_V :

$$\begin{cases} \Delta E_{KV} + \Delta E_V = \Delta E_{M5} - \Delta E_V \\ \Delta \alpha' = |\Delta E_{KV}| + \Delta E_{M5} = -\Delta E_{KV} + \Delta E_{M5} \\ \Delta \alpha' = \Delta E_{M5} - \Delta E_{KV} = 2\Delta E_V \end{cases} \quad (8)$$

The shift of the Auger parameter is assumed to be composed of two equal parts contributed from the involved two levels, where ΔR^{ex} is extra-atomic relaxation or polarization energy coming from the neighbor of core-ionized atom. The approximation is valid as long as the equal BE shift in all the levels involved in the definition of the Auger parameter is verified.⁹

2.3. Extended Wagner Plot. To effectively reflect the effects of electron rearrangement and final state screening and to obtain quantitative information, we extend the Wagner plot that is able to distinguish the effect of crystal-field screening (η_{MV}) from the effect of valence recharging (κ_{MV}), which is expressed as

$$\frac{E_V(K) - E_V(12)}{E_V(12) - E_V(0)} = \kappa_{MV} \frac{E_{M5}(K) - E_{M5}(12)}{E_{M5}(12) - E_{M5}(0)} \quad (9)$$

$$\eta_{MV} = \frac{E_V(12) - E_V(0)}{E_{M5}(12) - E_{M5}(0)} \quad (10)$$

The coefficient $\kappa_{MV} = 1$ if no chemical reaction occurs, which represents the effect of valence recharging, while η_{MV} , the screening coefficient, represents the ratio of binding intensity to the two levels in the bulk of elemental solid.

3. CALCULATION PROCEDURES

If there are a total of n components of bulk (B) and surface (S_i) involved in an XPS peak of the Ag solid skins, one should have a combination of $N = C_n^2 = n! / [(n-2)!2!]$ values of $E_v(0)$. One can find the mean $\langle E_v(0) \rangle$ with a standard deviation, σ ,

$$\begin{cases} \langle E_v(0) \rangle = [\sum_N E_{vi}(0)] / N \\ \sigma = \left\{ \sum_N [E_{vi}(0) - \langle E_v(0) \rangle]^2 / [N(N-1)] \right\}^{1/2} \end{cases} \quad (11)$$

The $E_{vi}(0)$ corresponds to $E_v(0)$ in eq 4 due to the combination of ($z \neq z'$). A fine-tuning of the z value or the peak energy for each component will minimize the value of σ , and hence, the $\langle E_v(0) \rangle$ approaches the true situation. The accuracy of the $E_v(0)$ and the $\Delta E_v(12)$ depends on the volume size of the database, i.e., how many sets of data (according to the number of z) collected from differently oriented skins of the same material. The Ag(100) and (111) skins contain each B, second surface (S_2), and first surface (S_1) components; there are a total of 5 components and $N = C_5^2 = 5! / [(5-2)!2!] = 10$ possible $E_v(0)$ values, and then, we can find their average and deviation.

The XPS spectra background correction needs to be carried out using the standard Tougaard method^{23,24} and Gaussian-type function before decomposition. The Gaussian type deconvolution would be sufficient and most convenient, as demonstrated. The corrected spectra are then normalized under the guideline of spectral area conservation, which means that the number of electrons emitted from the same specimen should be proportional to one another irrespective of experimental conditions. Such normalization aims to remove the artifacts due to scattering by variation of emission angle or incident beam energy. The atomic CN for each sublayer is the only adjustable parameter in decomposition.²⁵

According to the established constraints on the energy separation between each component, eq 3, each XPS spectrum is decomposed with the B and S_i components from higher (smaller value) to lower BE upon background correction and normalization. The number of components is referral to the reported outcome that is subject to the fitting to the spectral peak. The decomposition was conducted by choosing $z_1 = 4$ for the fcc (100) top layer^{26–28} as the standard reference. The rest of the z values for various sublayers and orientations of the same geometry are optimized collectively by fine-tuning the peak energy of the components of different materials.

4. RESULTS AND DISCUSSION

4.1. Ag Surface and Defect $3d_{5/2}$ BE Shift. On the basis of the developed approaches, we decomposed the measured $3d_{5/2}$ XPS spectrum from the (111)²⁹ and (100)³⁰ planes of

clean Ag surfaces displayed in Figure 2. The spectra were decomposed into the bulk (B), second surface (S_2), first surface (S_1), and defect (D) states from higher (smaller absolute value) to lower BE. These components follow the constraints of eq 3 with derived parameters given in Table 1.

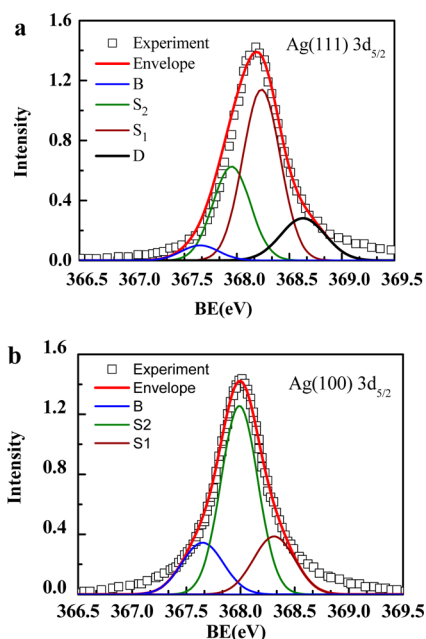


Figure 2. Decomposition of the Ag $3d_{5/2}$ spectra for (a) Ag(111)²⁹ and (b) Ag(100)³⁰ surfaces with four Gaussian components each representing the bulk B, surfaces S_2 and S_1 , and defects D states from higher (smaller absolute value) to lower BE. These components follow the constraints of eq 3 with derived parameters given in Table 1.

(S_1), and defect (D) components, respectively, from higher to lower BE. From the decomposition, we can obtain the values of $E_{3d_{5/2}}(0)$, $E_{3d_{5/2}}(B)$, and $E_{3d_{5/2}}(S_1)$, as summarized in Table 1. The

Table 1. Effective CNs (z), Local Lattice Strain ($\epsilon_z = C_z - 1$), BE Shift $\delta E_z = \Delta E(z)/\Delta E(12) - 1 = C_z^{-1} - 1$, Relative Atomic Cohesive Energy $\delta E_{\text{coh}} = E_{\text{coh}}(z)/E_{\text{coh}}(12) - 1 = z_{\text{ib}}C_z^{-1} - 1$, and the Relative BE Density $\delta E_{\text{den}} = E_{\text{den}}(z)/E_{\text{den}}(12) - 1 = C_z^{-4} - 1$ in Various Planes of the Same fcc Geometry and the $3d_{5/2}$ Peak Position of Each Component Derived from the XPS Spectra of Ag Surface Skins; Ag Shares the Same Effective CNs for fcc (100) and (111) with Pd and Rh

	z	Ag	$-\epsilon_z$ (%)	δE_z	δE_{den}	$-\delta E_{\text{coh}}$
atom	0	363.02				
bulk	B	12	367.65	0	0	0
(111) ²⁹	S_2	6.31	367.93	5.63	5.97	26.08
	S_1	4.26	368.24	11.31	12.75	61.60
	D	3.14	368.63	17.45	21.15	115.39
(100) ³⁰	S_2	5.73	367.99	6.83	7.33	32.70
	S_1	4.00	368.31	12.44	14.20	70.09

Table 2. Information Derived by Fitting Size Dependence of XPS and AES Lines of Ag Deposited on Al_2O_3 and on CeO_2 Substrates

		Al_2O_3	CeO_2
$E_{3d_{5/2}}$ (eV)	$E_{\text{MS}}(12)$	−367.59	−368.25
	$E_{\text{MS}}(0)$	−363.02	−363.02
	$\Delta E_{\text{MS}}(12)$	−4.63	−5.23
E_V (eV)	$E_V(12)$	−7.56	−8.32
	$E_V(0)$	−0.36	−0.36
	$\Delta E_V(12)$	−7.20	−7.96
E_K (MSVV) (eV)	$E_K(12)$	352.45	351.61
	$E_K(0)$	362.30	362.30
	$\Delta E_K(12)$	9.85	10.69
η_{MV} (screening coefficient)		1.56	1.50
κ_{MV} (recharging coefficient)		1.21	1.15

BE for an isolated atom is optimized to be 363.02 eV with their respective bulk shift of 367.65 eV. The $E_{3d_{5/2}}(0)$ and $E_{3d_{5/2}}(B)$ should be identical for all the surfaces and subsurface layers of Ag regardless of experimental or surface conditions.

In order to ensure the minimal error of the envelope spectra and the experimental spectra, fine-tuning of the z -values was performed in the decomposition. The optimized CN values of the top (111) and (100) atomic layers are 4.26 and 4.00, and the CNs for the corresponding second layer are 6.31 and 5.73 and are shown in Table 2. The presently optimized values for all the sublayers are identical to those derived from the same fcc surfaces of Pd and Rh.³¹ The consistency of the effective CN for both the fcc Pd, Rh, and Ag surfaces further confirmed the reliability of this approach in determining the effective CN for the surface layers. The findings in the current work lead to an expression for the z -resolved $3d_{5/2}$ core level shift for Ag

$$E_{3d_{5/2}}(z) = \langle E_{3d_{5/2}}(0) \rangle \pm \sigma + \Delta E_{3d_{5/2}}(12) C_z^{-1} = 363.022 \pm 0.008 + 4.628 C_z^{-1} \quad (12)$$

This fundamental information is of great importance in understanding the surface behavior of these under-coordinated atoms.

4.2. Further Derivatives. With the derived CN values z and the $3d_{5/2}$ binding energies for each surface component from the XPS spectra decomposition, one is able to predict the z -resolved local lattice strain, BE positive shift (potential trap depth), binding energy density, and cohesive energy per discrete atom in the Ag surface skins

$$\begin{cases} \epsilon(z) = C_z - 1 & (\text{local lattice strain}) \\ \delta E_z = \Delta E(z)/\Delta E(12) - 1 = C_z^{-1} - 1 & (\text{BE shift}) \\ \delta E_{\text{den}} = E_{\text{den}}(z)/E_{\text{den}}(12) - 1 = C_z^{-4} - 1 & (\text{binding energy density}) \\ \delta E_{\text{coh}} = E_{\text{coh}}(z)/E_{\text{coh}}(12) - 1 = z_{\text{ib}} C_z^{-1} - 1 & (\text{atomic cohesive energy}) \end{cases} \quad (13)$$

where $z_{\text{ib}} = z/12$ is the reduced CN, $z = 12$ is the bulk value, and $m = 1$ for metal. Therefore, we can extract information of the bond order (z), bond length (d), bond strength (E_z), the binding energy density (E_{den}), and atomic cohesive energy (E_{coh}) in the Ag(111) and (100) sublayers, as summarized in Table 1. Consistency between the BOLS predictions and the XPS derivatives has been achieved, as is shown in Figure 3.

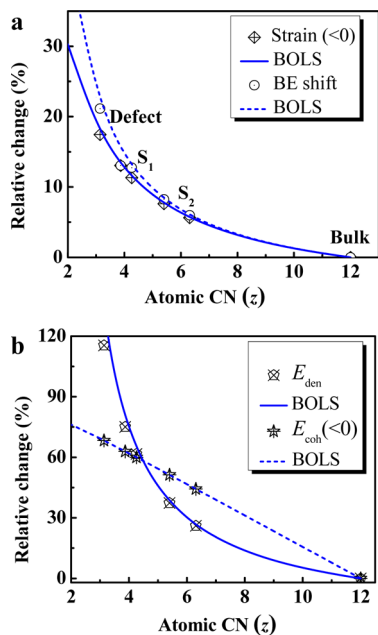


Figure 3. BOLS derived (solid curves) coordination number (z)-resolved (a) local bond strain and BE shift; (b) atomic cohesive energy E_{coh} and binding energy density E_{den} of the Ag bulk ($z = 12$) surface skins ($z = 4$ –6) and defect ($z < 4$).

These basic quantities determine the unusual physical and chemical properties of the low dimensional material. For example, the melting point³² of Ag nanoparticles decreases with the reduction of the particle size, while the Young's modulus³³ will show the opposite fashion, the reason behind this is that the Young's modulus is proportional to the binding energy density while the melting point is proportional to the atomic cohesive energy.³⁴

4.3. Ag Nanoparticle Valence BE Shift. To clarify the size effect on the shift of the $3d_{5/2}$, the MSVV, and the valence BE of Ag NPs, we first need to obtain the dimensionality τ and the bond nature indicator m . For Ag deposited on CeO₂ substrate, there is no charge transfer between the CeO₂ substrate and Ag nanoclusters.³⁵ So the bond nature indicator $m = 1$, remaining that of pure Ag.²⁸ According to eqs 6 and 7, a linear fitting to the measured data leads to $B = 5.567$ and $E_v(12) = 368.25$ eV from the plot of Ag $3d_{5/2}$ BE versus the inverse of K , which determined the shape factor $\tau = 1.45$.

Because of the same-shaped mode of 3D growth⁸ of Ag on CeO₂ and Al₂O₃ substrates, the value τ holds for both.²⁸ However, the bond nature of Ag derived from the experimental data altered because of charge transfer between Ag and the Al₂O₃ substrate.¹¹ Similarly, a linear fitting to the measured data results in B and $E_v(12)$ values. According to eqs 6 and 7, $m = 3.82$ for Ag on Al₂O₃ was determined. Actually, the $E_v(\infty)$ is a constant for a given material, but we can see that the $E_v(\infty)$ of Ag deposited on Al₂O₃ and CeO₂ is different, the reason of

which is why we should take some offset in analyzing the experimental results.

With the obtained values of m and τ , size dependence of the Ag $3d_{5/2}$ BE, the MSVV Auger electron kinetics energy, and the valence BE with Ag deposited on CeO₂ and Al₂O₃ substrates were determined as shown in Figure 4. Note that valence

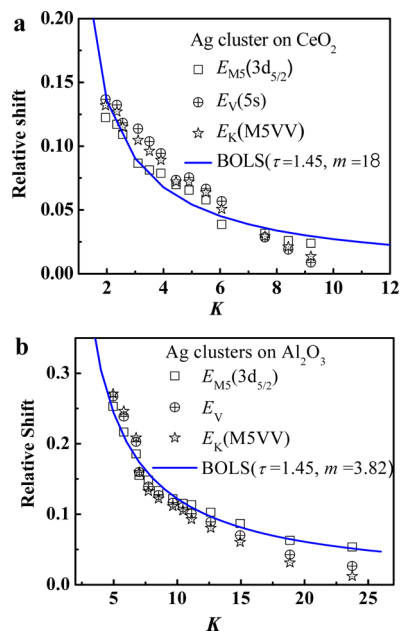


Figure 4. Theoretical reproduction (solid line) of the measured size dependence of E_{M5} , E_{V} , and E_{K} line of Ag particles deposited on (a) CeO₂³⁵ and (b) Al₂O₃⁸ substrates. τ is the dimensionality and m the bond nature indicator.

binding energy can be obtained by eq 6; the relative shift is the ratio of $\Delta E_v(K) - \Delta E_v(12)$ and $\Delta E_v(12)$, and K is proportional to the cube root of Ag coverage only with different coefficient³⁶ as on both the Al₂O₃ and CeO₂ substrates, Ag NPs grow in the 3D mode. It shows that the relative shifts of the $3d_{5/2}$, the valence, and the Auger kinetics energy increase when the size K decreases.

4.4. Extended Wagner Plot. With the data derived from the size dependence of the binding energy of $3d_{5/2}$ and valence levels, we also plot the extended Wagner plot of Ag on CeO₂ and Al₂O₃ substrates as is shown in Figure 5. The slope denotes the valence recharging effect, which is influenced by the interfacial interaction between Ag atoms and the substrate.²⁸ Ideally, the bond nature indicator should be $m = 1$ for metals.²⁸ However, the calculated results show $m = 3.82$ for Ag deposited on Al₂O₃. This indicates that the bond nature at the interface has altered, which agrees with the density functional calculation results.¹¹

Besides, as the BEs of the isolated atom as well as the their bulk shift have all been achieved from analyzing the size dependence of $3d_{5/2}$ and valence levels, the screening coefficients of Ag deposited on the Al₂O₃ and CeO₂ substrate are readily available as listed in Table 2. As can be seen from Table 2, the screening coefficients are 1.56 and 1.50 for Ag deposited on Al₂O₃ and CeO₂, respectively. Similar to the valence recharging coefficient, different substrates give different screening coefficients, suggesting that the interfacial interaction between the Ag and the substrates also affects the electron screening of the core level and valence levels.

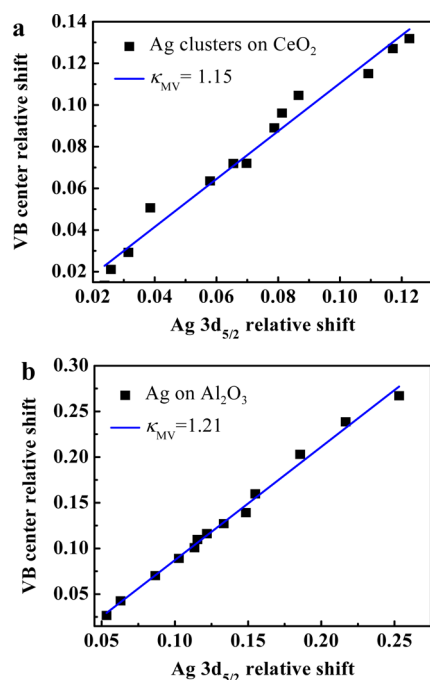


Figure 5. Extended Wagner plot showing the correlation between the relative shift of valence level and the $3d_{5/2}$ of Ag clusters deposited on (a) CeO_2 ³⁵ and (b) Al_2O_3 ⁸ substrates. The κ_{MV} is the slope of the correlation representing the valence recharging effect due to chemical reaction.

5. CONCLUSIONS

We analyzed the coordination resolved Ag $3d_{5/2}$ surface energy shift and the size dependence of Ag MSVV AES shift, $3d_{5/2}$, and valence XPS shifts of Ag deposited on CeO_2 and Al_2O_3 substrates based on the BOLS–TB method. Results show that the $3d_{5/2}$ and the valence band shift positively when the CN is reduced or the interface interaction becomes dominant, which is ascribed to the Hamiltonian perturbation induced by the local quantum entrapment and the heterocoordinated interface effect. Consistency between the predicted result and experimental data demonstrate the validity of the approaches, which enable us to distinguish the electron screening effect from the electron recharging effect.

AUTHOR INFORMATION

Corresponding Author

*E-mail: ywang8@hust.edu.cn (Y.W.); ecqsun@ntu.edu.sg (C.Q.S.).

Notes

The authors declare no competing financial interest.

ACKNOWLEDGMENTS

This work was supported by National Natural Science Foundation of China (Nos.11172254 and 11002121), the Key Special Program for Science and Technology of Hunan Province (No. 2009FJ1002), and MOE (RG15/09), Singapore.

REFERENCES

- (1) Armstrong, J. N.; Hua, S. Z.; Chopra, H. D. *Phys. Status Solidi RRL* **2012**, *9*, 99–101.
- (2) Roy, D.; Barber, Z. H.; Clyne, T. W. *J. Appl. Phys.* **2002**, *91* (9), 6085.
- (3) Pal, S.; Tak, Y. K.; Song, J. M. *Appl. Environ. Microbiol.* **2007**, *73* (6), 1712–1720.
- (4) Farmer, J. A.; Baricuatro, J. H.; Campbell, C. T. *J. Phys. Chem. C* **2010**, *114* (40), 17166–17172.
- (5) Branda, M. A. M.; Hernández, N. C.; Sanz, J. F.; Illas, F. *J. Phys. Chem. C* **2010**, *114* (4), 1934–1941.
- (6) Luches, P.; Pagliuca, F.; Valeri, S.; Illas, F.; Preda, G.; Pacchioni, G. *J. Phys. Chem. C* **2012**, *116* (1), 1122–1132.
- (7) Luo, K.; St. Clair, T. P.; Lai, X.; Goodman, D. W. *J. Phys. Chem. B* **1999**, *104* (14), 3050–3057.
- (8) Luo, K.; Lai, X.; Yi, C. W.; Davis, K. A.; Gath, K. K.; Goodman, D. W. *J. Phys. Chem. C* **2005**, *109* (9), 4064–4068.
- (9) Giuliano, M. *Spectrosc. Relat. Phenom.* **1998**, *95* (2–3), 95–144.
- (10) Masahide, O. *Spectrosc. Relat. Phenom.* **2004**, *136* (3), 229–234.
- (11) Hernández, N. C.; Graciani, J.; Márquez, A.; Sanz, J. F. *Surf. Sci.* **2005**, *575* (1–2), 189–196.
- (12) Rodríguez, J. A.; Kuhn, M.; Hrbek, J. *J. Phys. Chem.* **1996**, *100* (46), 18240–18248.
- (13) Li, J. W.; Ma, S. Z.; Liu, X. J.; Zhou, Z. F.; Sun, C. Q. *Chem. Rev.* **2012**, *112*, 2833–2852.
- (14) Sun, C. Q. *Phys. Rev. B* **2004**, *69* (4), 045105.
- (15) Sun, C. Q.; Sun, Y.; Nie, Y. G.; Wang, Y.; Pan, J. S.; Ouyang, G.; Pan, L. K.; Sun, Z. *J. Phys. Chem. C* **2009**, *113* (37), 16464–16467.
- (16) Omar, M. A., *Elementary Solid State Physics: Principles and Applications*; Addison-Wesley: New York, 1993.
- (17) Goldschmidt, V. *Ber. Dtsch. Chem. Ges.* **1927**, *60* (5), 1263–1296.
- (18) Pauling, L. *J. Am. Chem. Soc.* **1947**, *69* (3), 542–553.
- (19) Frick, B.; Jacobi, K.; Meyer, G.; Henzler, M. *Solid State Commun.* **1987**, *63* (6), 475–479.
- (20) Montano, P. A.; Zhao, J.; Ramanathan, M.; Shenoy, G. K.; Schulze, W.; Urban, J. *Chem. Phys. Lett.* **1989**, *164* (2–3), 126–130.
- (21) Yang, D. Q.; Sacher, E. *Appl. Surf. Sci.* **2002**, *195* (1–4), 187–195.
- (22) Pan, L. K.; Sun, C. Q.; Li, C. M. *Appl. Surf. Sci.* **2005**, *240* (1–4), 19–23.
- (23) Hajati, S.; Coultas, S.; Blomfield, C.; Tougaard, S. *Surf. Sci.* **2006**, *600* (15), 3015–3021.
- (24) Seah, M. P.; Gilmore, I. S.; Spencer, S. J. *Surf. Sci.* **2000**, *461* (1–3), 1–15.
- (25) Wang, Y.; Nie, Y. G.; Wang, L. L.; Sun, C. Q. *J. Phys. Chem. C* **2010**, *114* (2), 1226–1230.
- (26) Fang, B. S.; Lo, W. S.; Chien, T. S.; Leung, T. C.; Lue, C. Y.; Chan, C. T.; Ho, K. M. *Phys. Rev. B* **1994**, *50* (15), 11093–11101.
- (27) Bartynski, R. A.; Heskett, D.; Garrison, K.; Watson, G.; Zehner, D. M.; Mei, W. N.; Tong, S. Y.; Pan, X. *J. Vac. Sci. Technol., A* **1989**, *7* (3), 1931–1936.
- (28) Sun, C. Q. *Prog. Solid State Chem.* **2007**, *35* (1), 1–159.
- (29) Andersen, J.; Hennig, D.; Lundgren, E.; Methfessel, M.; Nyholm, R.; Scheffler, M. *Phys. Rev. B* **1994**, *50* (23), 17525–17533.
- (30) Rocca, M.; Savio, L.; Vattuone, L.; Burghaus, U.; Palomba, V.; Novelli, N.; Buatier de Mongeot, F.; Valbusa, U.; Gunnella, R.; Comelli, G.; Baraldi, A.; Lizzit, S.; Paolucci, G. *Phys. Rev. B* **2000**, *61* (1), 213.
- (31) Wang, Y.; Nie, Y. G.; Pan, J. S.; Pan, L. K.; Sun, Z.; Wang, L. L.; Sun, C. Q. *Phys. Chem. Chem. Phys.* **2010**, *12* (9), 2177–2182.
- (32) Jiang, Q.; Zhang, S.; Zhao, M. *Mater. Chem. Phys.* **2003**, *82* (1), 225–227.
- (33) Moon, K.-S.; Dong, H.; Maric, R.; Pothukuchi, S.; Hunt, A.; Li, Y.; Wong, C. J. *Electron. Mater.* **2005**, *34* (2), 168–175.
- (34) Liu, X. J.; Zhou, Z. F.; Yang, L. W.; Li, J. W.; Xie, G. F.; Fu, S. Y.; Sun, C. Q. *J. Appl. Phys.* **2011**, *109* (7), 074319–074315.
- (35) Kong, D.; Wang, G.; Pan, Y.; Hu, S.; Hou, J.; Pan, H.; Campbell, C. T.; Zhu, J. *J. Phys. Chem. C* **2011**, *115* (14), 6715–6725.
- (36) Argile, C.; Rhead, G. E. *Surf. Sci. Rep.* **1989**, *10* (6–7), 277–356.